ACS APPLIED ENERGY MATERIALS

www.acsaem.org Article

A Nonaqueous Eutectic Electrolyte for Rechargeable Iron Batteries

Raju Vadthya, Nikhitha Poornabodha, Hao Nguyen, Olumide Oladoyin, Sergei A Ivanov, Houlong Zhuang, and Shuya Wei*

Cite This: ACS Appl. Energy Mater. 2024, 7, 3876−3887 Read Online

ACCESS | Metrics & More | Article Recommendations | Supporting Information

ABSTRACT: Iron metal has attracted great interest as an anode material for the development of aqueous rechargeable batteries due to its huge abundance in the earth's crust, offering significantly lower cost per cell. However, the intractable side reactions at the negative iron anode and parasitic hydrogen evolution in aqueous media hamper the technology being unattainable for practical evaluations. Herein, we demonstrate a nonaqueous, eutectic electrolyte based on triethylamine hydrochloride ($(Et_3NH)Cl$) and $FeCl_3$ as an efficient electrolyte for the application of rechargeable iron batteries (RIBs). The eutectic formation is achieved by dual intermolecular interactions, namely, Lewis acid−base interactions and hydrogen bonding, resulting in hybrid organic−inorganic active ionic complex species. The optimized eutectic electrolyte offers appreciably high ionic conductivity (~1.2 mS cm^{-1}) at room temperature, high plating and stripping efficiency (~100%), a long cycling stability of ≅400 h in a symmetric iron cell, and a wide operating potential window (~2.5 V on Mo or carbon-coat Al). Differential scanning calorimetry (DSC) reveals that the electrolyte renders the liquid phase at −11 °C. A hydrothermally synthesized V_2O_5 nanowire cathode paired against an iron anode in the optimized eutectic electrolyte renders a good capacity of ~140 mAh g^{-1} at a current density of 10 mA g^{-1}. The charge storage mechanism of the cell is thoroughly investigated by X-ray photoelectron spectroscopy (XPS) and X-ray diffraction on the galvanostatically cycled electrodes. The addition of $AlCl_3$ extends the electrolyte stability window to 3.2 V on SS, resulting in enhanced cell performance that maintains stability for >100 cycles. This work introduces a eutectic electrolyte class that can enable safe RIBs at low-cost and a wide operating potential window.

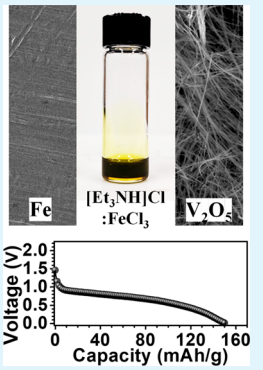

KEYWORDS: *eutectic, electrolytes, iron, rechargeable batteries, V_2O_5*

INTRODUCTION

Renewable energy sources are essential for achieving a carbon-free biosphere and tackling the energy crisis. However, the unequal distribution and intermittency of these resources require the integration of large-scale energy storage systems to store and deliver on demand. Li-ion batteries have shown remarkable achievements, including high cell voltage (~3.6−4 V per cell), long cyclability, high energy density (~150 Wh kg^{-1}), and stability at all climate conditions (−40 °C to +70 °C). However, their widespread adoption for grid-storage and electric vehicles is impeded by the thermal instability of organic solvents in the electrolytes, as well as issues related to cost-effectiveness and the availability of resources.[1−3] Multivalent metal batteries have emerged as one of the promising alternatives to surpass the challenges posed by Li-ion technology due to their ability to transfer multiple electrons per single ion de/intercalation, thereby increasing the volumetric energy density by two- or threefold.[4,5] Mg, Al, Zn, Ca, etc,. have been extensively researched in the past decade due to their huge abundance in the earth's crust, multiple electrons transfer upon red-ox reactions, nontoxic, and remarkably high theoretical capacity.[5,6] Iron, a typical multivalent metal, is often overlooked as an anode for the design of rechargeable batteries due to its relatively high standard red-ox potential value (−0.44 V).[7] However, iron offers advantages such as robustness, nontoxicity, environmental benignity, and a huge presence in the earth's crust (5.63 wt % vs. 0.002 wt % for Li), and significantly lower cost (0.06 USD kg^{-1} vs. 19.2 USD kg^{-1} for Li).[8,9] Iron chemistry offers eight oxidation states (i.e., −2 to +6), a high theoretical capacity (of ~7558 mAh cm^{-3} and ~1440 mAh g^{-1} for $3e^-$ transfer), and nondendritic growth upon cycling predisposes iron as an attractive contender for large scale energy storage systems.[8,10]

Edison et al. reported an aqueous iron−nickel battery that exhibited a high energy density (~19−25 Wh kg^{-1}) and a robust performance under abusive conditions such as overcharging, overdischarging, or short-circuiting.[10] However, the superior energy output and faster cyclability of lead-acid batteries overtook the market and obliviated iron−nickel chemistry from commercial space. In the past decade, iron metal chemistry has regained interest in the design of safe,

Received: January 30, 2024
Revised: April 16, 2024
Accepted: April 17, 2024
Published: April 25, 2024

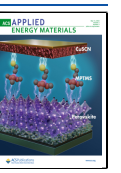

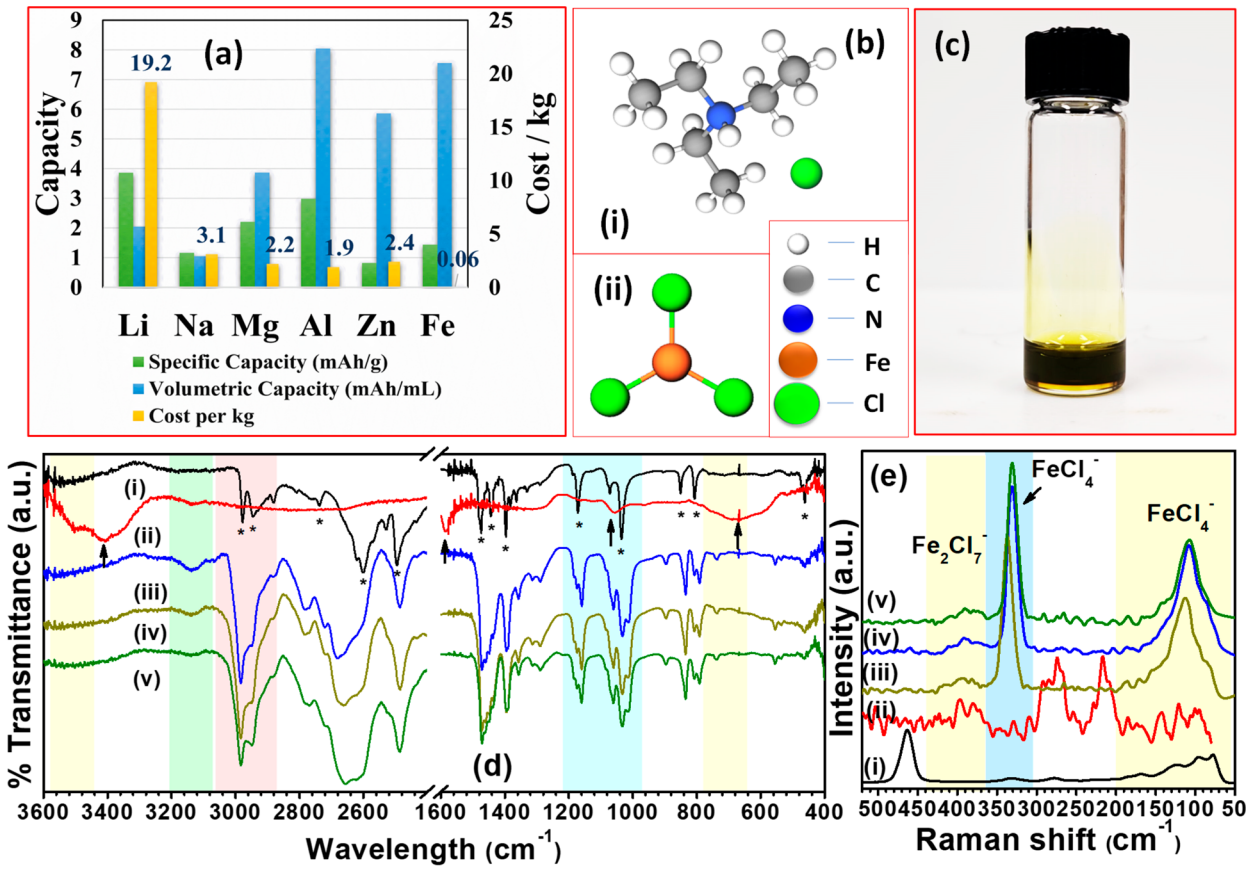

Figure 1. (a) Comparison of theoretical capacities and price of various mono- (Li and Na) and multivalent (Mg, Al, Zn, and Fe) metal anodes. (b) Chemical structures of (i) triethylamine hydrochloride and (ii) iron(III) chloride. (c) Pictorial depiction of the eutectic electrolyte formed between $(Et_3NH)Cl$ and $FeCl_3$. Representative FTIR stack plots of the pure and as-prepared eutectic compositions in the spectral ranges of 3600 cm^{-1} to 400 cm^{-1} is presented in (d). (e) Raman signals obtained for the samples confirming the active ionic complexes present: (i) $(Et_3NH)Cl$, (ii) $FeCl_3$, and the eutectics formed between the two composition at different molar ratios of (iii) 1.6:1, (iv) 1.7:1, and (v) 1.8:1 of $(Et_3NH)Cl$:$FeCl_3$.

high-energy density, and nontoxic batteries for grid storage applications. However, in aqueous electrolyte media, the charge storage behavior of iron-ion battery is influenced by the electrolyte formulation, pH, and the formation of nonconductive passivation leading to less cyclability and poor plating/stripping of iron originating from the parasitic hydrogen evolution.[11] Nonetheless, the literature is dedicated to improving iron-ion battery performance by storing Fe^{2+}-ions within diverse hosts such as $VOPO_4{\cdot}2H_2O$, phenylamine intercalated-$VOPO_4$, and cross-linked polyaniline, employing aqueous electrolytes. However, the operational potential window of the cell remains limited to ≤1.4 V vs Fe/Fe^{2+}.[12−14] Numerous attempts have been devoted to overcome the inherent difficulties presented by aqueous electrolytes for iron-ion battery. These endeavors involve developing non-aqueous electrolytes that possess broad operational thermal and potential ranges, low volatility, and high ionic conductivity. In 2019, Ajay et al. reported iron-ion battery in an ether-based electrolyte (i.e., hydrated $Fe(ClO_4)_2$ in tetraethylene glycol dimethyl ether). The key feature of their concept was the electrolyte's ability to operate in a wide operational potential window (0.0−2.0 V) with a high discharge capacity (~207 mAh g^{-1} at 30 mA g^{-1}) using a V_2O_5 cathode as an intercalation host.[15] Later, Zhao et al. investigated 1-butyl-3-methylimidazolium tetrachloroferrate as a promising charge carrier medium for the iron-graphite battery.[16] Interestingly, the negative discharge voltage at −0.2 V is attributed to the unclear mechanism of iron plating/stripping of chloroferrate ions de/intercalation, which requires further investigation to elucidate.

In this study, we attempted to devise a new class of electrolytes composed of $(Et_3NH)Cl$ and $FeCl_3$ for iron-ion battery application. This electrolyte belongs to the class of deep eutectics, which are akin to ionic liquids. The electrolyte offers superior advantages such as wide thermal and electrochemical stability, fast ionic diffusion facilitated by the weakly coordinating ionic solvation, and cost-effectiveness due to the facile synthetic process with high-yield. The dual intermolecular interactions that govern the binary-phase eutectic formation are comprehensively investigated using Fourier transform infrared (FTIR) and Raman spectroscopic techniques. The optimized eutectic exhibited an appreciably high ionic conductivity (~1.2 mS cm^{-1}) at room temperature (RT), efficient iron plating/stripping efficiencies (>82% on SS 316 plate and Mo), wide electrochemical stability window (~2.5 V), and long-term cycling stability (>400 h). Notably, the high anionic transport number of the eutectics close to unity strongly infers the dominating role of mono- or divalent iron-chloride complexes in iron redox reactions. V_2O_5, synthesized via hydrothermal routes, offers nanowire morphology with an average diameter of ~0.3 μm. When paired with the Fe anode, the V_2O_5 cathode manifests a capacity of ~140 mAh g^{-1} at a current density of ~10 mA g^{-1}. The eutectic electrolytes offer a promising strategy to conceptualize and formulate nonaqueous

https://doi.org/10.1021/acsaem.4c00263
ACS Appl. Energy Mater. 2024, 7, 3876−3887

electrolytes for the sophisticated multivalent metal anodes that are often plagued by poor electroplating/stripping performance such as iron.

RESULTS AND DISCUSSION

The ubiquity of iron has been immensely popular since the Bronze Age. Despite iron's competitive theoretical capacity (7558 mAh cm^{-3} for $3e^-$ transfer) and small ionic size (~76 pm for Fe^{2+}, ~65 pm for Fe^{3+} vs. ~90 pm for Li^+), iron electrochemistry pertaining to energy harvesting is still in its infant stage. On the downside, high gravimetric density of iron, i.e., ~7.9 g cm^{-3} (vs. 0.53 g cm^{-3} for Li) is detrimental to the fast diffusion kinetics of the charge carriers. To suppress the negative effect, a new strategy was followed to develop an electrolyte that gives rise to new redox process chemistries between the charge carriers and the electrodes. The ammonium salt, $(Et_3NH)Cl$ has a tabulated melting point (T_m) of ~533 K and $FeCl_3$ has a T_m of ~579 K. However, $FeCl_3$ acts as a Lewis acid when mixed with a nucleophile and a hydrogen bond donor $(Et_3NH)Cl$ at room temperature (T_{RT} ~ 298 K), leading to the significant lowering of the melting point. Owing to an increase in entropy, the system undergoes a phase transition from solid to liquid due to strong hydrogen bonding interactions, which leads to poor selectivity in molecular binding.[17] A series of binary eutectic compositions were prepared iteratively by varying the molar ratio of $(Et_3NH)Cl$ to $FeCl_3$. The ratio was varied from 1.5:1 to 2.0:1 with 0.1 increment, in all cases resulting in a clear liquid phase with no sediment after keeping the solution undisturbed for 72 h at RT. However, at ratios 1.5:1, 1.9:1, and 2.0:1 $(Et_3NH)Cl:FeCl_3$, the mixture displays high viscosity (gel-like) texture at RT. Hence, our investigation was limited to the remaining ratios 1.6:1, 1.7:1, and 1.8:1 to optimize the *physicochemical* and electrochemical properties for iron-ion battery applications.

Vibrational spectroscopic techniques such as Fourier Transform Infrared (FTIR) and Raman spectroscopies were employed to understand the following characteristic features that cause the eutectic formation: (i) hydrogen bonding interactions, (ii) key ionic complexes, (iii) free ions, and (iv) ion clusters present in the binary eutectic compositions. Typical FTIR spectra of pure $(Et_3NH)Cl$, as shown in Figure 1(d)-(i), denote all the characteristic peaks corresponding to ν_{C-H} and ν_{C-N} stretches in the frequency range of 3050−2850 cm^{-1} and 1200−1000 cm^{-1}, respectively.[18,19] $FeCl_3$ shows characteristic Fe−Cl stretching vibrations at ~400−300 cm^{-1}, typically identified as far-IR radiation range.[20] The FTIR spectra of all the eutectic compositions have shown considerable changes from pure $(Et_3NH)Cl$ or $FeCl_3$. Hence, the investigation of the electrolytes involves examining the potential interactions between two solid compositions that result in a phase transition.**(i) Hydrogen bonding interactions:** $(Et_3NH)Cl$ displays a weak band at ~2735 cm^{-1}, which corresponds to ν(H−Cl).[19,21] N−H stretching vibrations typically fall in the region of 3500−3400 cm^{-1}; however, a broad peak centered at ~3536 cm^{-1} is observed for $(Et_3NH)Cl$, which could be attributed to N−H stretching vibrations.[19,22,23] The FTIR spectra of all series of eutectics detect the shift in the N−H stretching vibrational band to ~3175−3099 cm^{-1}. This could attribute to the hydrogen bonding or interaction with the newly formed mono- or poly chloroferrate ions from the eutectics.[24,25] Additionally, ν(H−Cl) shows considerable shift toward lower frequency region *i.e.*, ~2718 cm^{-1} with suppressed intensity indicates the reduced participation of bonding. $[(C_2H_5)_3NH]$-Cl interacts with $FeCl_3$ and forms $((C_2H_5)_3N-H)^+$ and other chloroferrate ionic complexes. However, the shift in ν(H−Cl) for the eutectics defines the weak hydrogen bonding interaction between the $((C_2H_5)_3N-H)^+$ and chloroferrate complexes. **(ii) Ionic complexes:** The spectral bands corresponding to ν_{C-N} stretch (~1036 and 1072 cm^{-1}), *in-plane* methyl C−H bending motion (~1172 and 1188 cm^{-1}), and C−H bending mode of vibrations (~1443 cm^{-1}, 1474 and 1481 cm^{-1}) shift toward the lower frequency region while the peaks corresponding to CH_2 twisting vibrations (~1383 cm^{-1}), CH_2 symmetric stretch (~2736 cm^{-1}), and C−H asymmetric stretching vibrations of ethyl and methyl functional groups (~2946 cm^{-1}, ~2979 cm^{-1}) shift toward a higher frequency range.[19,26] The difference in spatial charge distribution among the alkyl side chain containing a quaternary ammonium cation may be attributed to the presence of highly polarized charge distribution in the environment. This polarization causes changes in the vibrational bond energy. The frequency change of any bond is observed to depend on the force constant and is given by $\nu = (1/2\pi c)(\sqrt{(k/\mu)})$ where ν is frequency, c is the speed of the light, k is the force constant, and μ is reduced mass. The shift toward lower frequency indicates a decrease in the force constant and a weakening of the bond. **(iii) Ionic clusters:** The presence of ionic clusters in the electrolyte solutions has an adverse effect on battery performance due to intermolecular hydrogen bonding between the similar ionic groups, which reduces the number of charge carriers. The transition of ν(H−Cl) toward the low-frequency region with reduced intensity indicates the possible presence of free-ionic pairs and ion aggregates in the eutectic.

To further understand the ionic complex species formed in the eutectic electrolyte, Raman spectra were acquired in the range of 500−50 cm^{-1}, as shown in Figure 1(e). The stack plots correspond to pure $(Et_3NH)Cl$) and $FeCl_3$ along with the series of eutectic electrolytes that retained the liquid phase at T_{RT}. Raman spectroscopy of eutectics showcases more characteristic peaks corresponding to the key ionic complexes formed in the range 500−50 cm^{-1}. Two sharp peaks observed at ~180−80 cm^{-1} and 310−345 cm^{-1} denotes the formation of tetrachloroferrate ($FeCl_4^-$).[27] As evidenced from the FTIR spectra, $FeCl_3$ presence induces a strong physical bond formed between N−H, and leads to the formation of quaternary ammonium ion, *i.e.*, $((C_2H_5)_3N-H)^+$, which is indexed in the range 2850−3000 cm^{-1} from the Raman spectra (shown in Figure SI4).[28] It is likely that the counterion in the eutectics is tetrachloroferrate, which is a weak hydrogen bond acceptor.[29] Another peak in the lower frequency region at 420−360 cm^{-1} is likely to correspond to the poly nuclear complex $Fe_2Cl_7^-$, formed by chloride bridging of two $FeCl_3$ units.[29,30] The eutectics with 1.7:1 $(Et_3NH)Cl:FeCl_3$ composition shows the prominent shift of peaks toward higher frequency, which represents the acidity of the ionic complexes formed. The presented FTIR and Raman data are consistent with the presence in the electrolyte of mono- and binuclear iron chloride complexes together with triethylammonium cation.

Further, the formation of active tetrachloroferrate ions is visualized by using the 2D charge density contour plots. A supercell consisting of $(Et_3NH)Cl$ and three $FeCl_3$ layers was modeled and optimized, as shown in Figure 2(a). Three planes, namely, Plane 1, Plane 2, and Plane 3, intersecting the Cl^- ions and Fe and Cl atoms in the $FeCl_3$ layers, have been

https://doi.org/10.1021/acsaem.4c00263
ACS Appl. Energy Mater. 2024, 7, 3876−3887

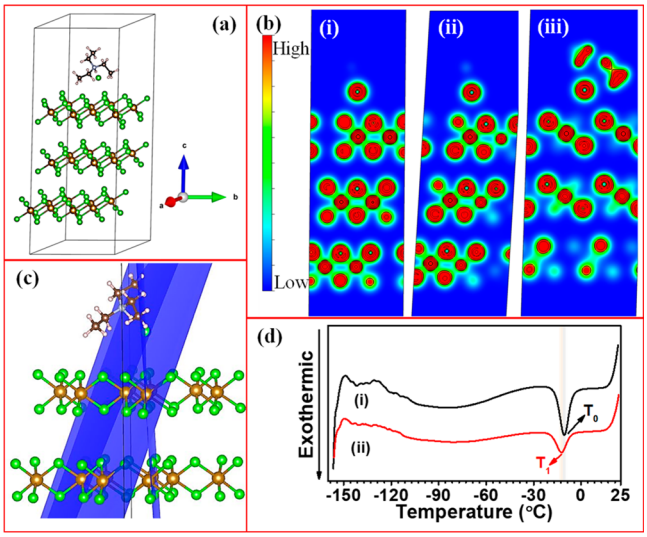

Figure 2. (a) Optimized structures of the atomic system consisting of $(Et_3NH)Cl$ and three $FeCl_3$ layers. (b) Representative 2D charge density contour plots of the atomic system, corresponding to the plates 1, 2, and 3 are shown in (i), (ii), and (iii), respectively. The red area corresponds to high electron density, whereas the blue area corresponds to low electron density. (c) Above three planes intersecting the Cl^-, Fe, and Cl atoms of the atomic system. (d) Thermograms of (i) 1.7:1 molar ratio of $(Et_3NH)Cl$:$FeCl_3$ and (ii) 1.8:1 molar ratio of $(Et_3NH)Cl$:$FeCl_3$.

selected to study the charge density distribution. The resultant 2D charge density contours of this atomic arrangement are displayed in Figure 2(b)-(i), (ii), and (iii) corresponding to Plane 1, 2, and 3, respectively. Figure 2c provides a comprehensive depiction of all three intersecting planes within the system, and Cl^-, Fe and Cl atoms display high electron density, indicating the interactions between Cl^- and $FeCl_3$ layers, potentially facilitating the formation of $FeCl_4^-$.

Differential Scanning Calorimetry (DSC) measurements were conducted within a temperature range of 25 °C to −150 °C for 1.7:1 and 1.8:1 molar ratio of $(Et_3NH)Cl$:$FeCl_3$, as depicted in Figure 2 (d)-(i) and (ii), respectively. Both eutectics underwent a phase transition from liquid to solid below 0 °C. The freezing points observed for 1.7:1 and 1.8:1 molar ratios of $(Et_3NH)Cl$:$FeCl_3$ were $T_0 \cong -10.6$ °C and $T_1 \cong -12.4$ °C, respectively. The presence of molecular interactions in the deep eutectic electrolytes (DEEs) facilitated the maintenance of liquid phase at low temperature, allowing the battery to operate over a broad temperature range.

For successful battery operation, electrolytes should possess a low viscosity, high ionic conductivity, and fast charge mobility under applied potential or current bias. Electrochemical impedance spectroscopy (EIS) was employed on a series of eutectics to estimate the bulk resistance and gain insight into the nature of the electrolyte conductivity. Typical Nyquist complex-plane plots of all eutectics are shown in Figure 3(a), recorded in the frequency range of 1 MHz to 1 kHz at an amplitude of ±10 mV. The conductivity is determined using the following equation; $\sigma = d/(R_bA)$, where σ is the ionic conductivity (in S cm^{-1}), d is the distance between the blocking electrodes (in cm), R_b is the bulk resistance measured from the EIS study (in Ohm) and A is the area of the blocking electrodes (in cm^2). The composition with 1.7:1 molar ratio displays the highest conductivity of ∼1.2 mS cm^{-1} in the series of studied electrolytes, whereas the remaining compositions with ratios 1.6:1, 1.8:1, 1.9:1, and 2.0:1 had conductivities of ∼0.89 mS cm^{-1}, ∼0.89 mS cm^{-1}, 0.69 mS cm^{-1}, and 0.64 mS cm^{-1}, respectively. The conductivity of eutectic solutions obtained in our work is comparable to ionic liquid electrolytes used in other multivalent metal batteries.[31,32] Wagner's dc polarization technique was employed on the eutectics by fabricating a symmetric cell containing SS 316 blocking electrodes to determine the ionic and electronic transport numbers. The representative plots of chronoamperometry at a constant potential of 100 mV and 1 V are shown in Supporting Information (Figure S1). A constant potential bias of 100 mV shows a poor ionic transport number of $t_{ionic} \cong 0.29$; however, an increase in the potential bias to 1 V tremendously increases its ionic transport character to ∼0.99. A similar trend in the transport behavior was observed for the remaining series of electrolyte solutions. Such characteristic behavior could be rationalized on the grounds of the high gravimetric densities of the ionic complexes, thus requiring high potential bias to induce ion acceleration toward the polarized plates. Ionic transference numbers in any metal-ion batteries play a vital role in realizing high-performance batteries and enable fast kinetics governed by high transference numbers.[33] Evan's method of dc polarization technique coupled with EIS measurement before and after the polarization applied to the series of eutectics provides crucial information on the ionic transference numbers present in the solution, as shown in the Supporting Information (Figures S2 and S3). An asymmetric cell comprising Fe||SS 316 was fabricated to investigate the transference numbers by using the following equation.

$$t^+ = (i_s/i_0)(\Delta V - R_0{}^* i_0)/(\Delta V - R_s{}^* i_s)$$

Here, i_0 and i_s are the respective current measured at the beginning and end of the polarization, ΔV is the applied potential bias to measure the current response with time, R_0 and R_s are the resistance of the cell from EIS plots measured before and after the polarization technique, respectively.[34] The deduced cationic and anionic transference numbers of all the series of eutectics at the applied potential bias of 100 mV and 1 V renders $t_{anionic} > 0.9$ and $t_{cationic} < 0.1$ (as tabulated in Table-SI 1). Here, t^- or $t_{anionic}$ can be referred to t_{FeCl4-} or $t_{Fe2Cl7-}$, and t^+ or $t_{cationic}$ is referred to as t_{Et3NH+}. Anionic transference number of 1.7:1 $(Et_3NH)Cl$:$FeCl_3$ renders ∼0.99, which is close to unity defines that the ionic conductivity is mainly accomplished by anions, *i.e.*, tetrachloroferrate or heptachloroferrate ions. This high number is anticipated to reduce the concentration polarization to deliver better electrochemical performance of a cell.

Despite the promising characteristic features of iron anode, the electrolyte's ability to potentially plate/strip iron without forming any inactive passivation leading to the failure of the battery is equally important. Initially, the successful plating-stripping property of the electrolyte is investigated using the cyclic voltammetry (CV) technique. CV studies were performed on the Fe||1.7:1-$(Et_3NH)Cl$:$FeCl_3$||SS 316 cell in the potential window of −0.5−0.5 V, at a slow scan rate of 0.5 mV s^{-1}, as shown in Figure 3 (b). The CV results demonstrate the reversible plating and stripping of iron metal in the eutectic electrolyte. However, iron plating is observed to dominate the redox process in the first few cycles. The potentiodynamic technique reveals similar results of successful plating and stripping efficiency for other eutectics, as shown in Figure S5. Further, the anodic stability of the electrolyte is investigated by

https://doi.org/10.1021/acsaem.4c00263
ACS Appl. Energy Mater. 2024, 7, 3876−3887

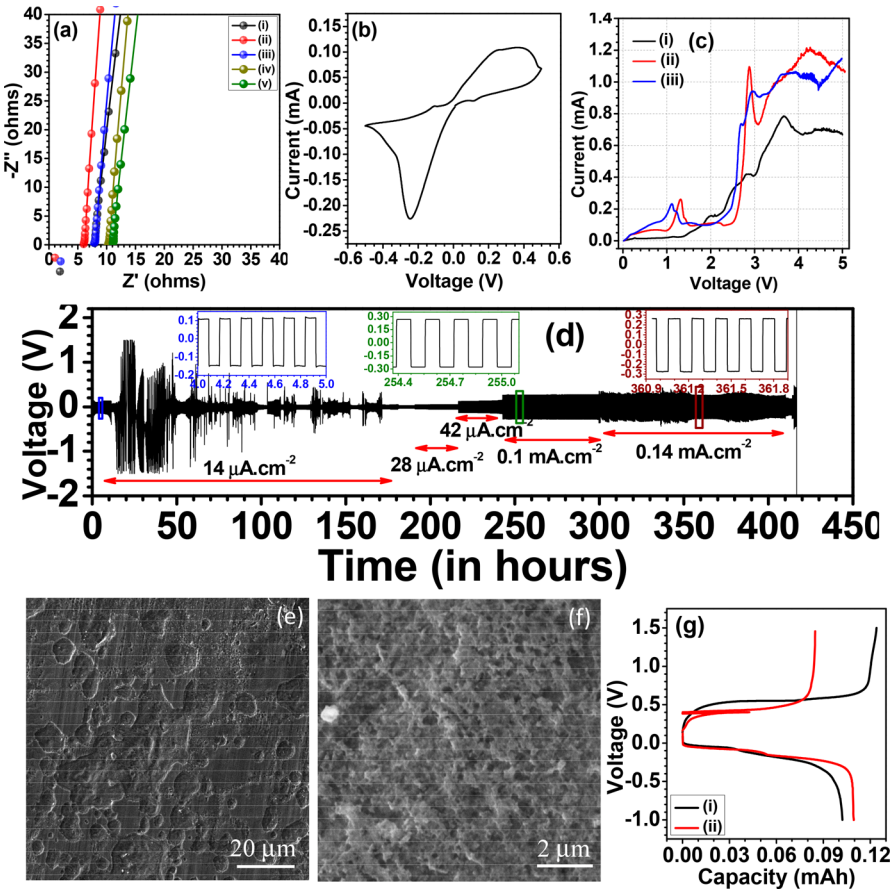

Figure 3. (a) Representative electrochemical impedance spectra recorded for the eutectics in the frequency range of 1 MHz to 100 mHz; (i), (ii), (iii), (iv), and (v) corresponds to 1.6:1, 1.7:1, 1.8:1, 1.9:1, and 2.0:1 of $(Et_3NH)Cl:FeCl_3$, respectively. (b) Typical cyclic voltammetry recorded on a Fe/1.7:1-$(Et_3NH)Cl:FeCl_3$/SS 316 plate in the voltage range of −0.5−0.5 V at the slew rate of 0.5 mV s^{-1}, depicts the Fe stripping and plating. (c) Linear sweep voltammetry recorded on different conductive substrates to decipher the potential stability window of the eutectic electrolyte (1.7:1-$(Et_3NH)Cl:FeCl_3$); (i) SS 316 plate, (ii) carbon-coat Al, and (iii) Mo. (d) Galvanostatic plating/stripping in a Fe||Fe symmetric cell in 1.7:1-$(Et_3NH)Cl:FeCl_3$ under different current densities. Inset images correspond to the enlarged view of plating/stripping at different time intervals. Representative SEM micrographs taken for the counter and working electrode post galvanostatic plating/stripping are shown in (e) and (f) respectively. (g) Galvanostatic stripping followed by plating performed on the asymmetric Fe||Mo cell at 0.09 $mA.cm^{-2}$ (i) and 0.18 $mA.cm^{-2}$ (ii).

fabricating a two-electrode cell setup, having iron as a counter electrode (CE) and SS 316 or carbon-coat Al or Mo plate as a working electrode (WE) in 1.7:1 $(Et_3NH)Cl:FeCl_3$ electrolyte. Linear sweep voltammetry (LSV) was performed to determine the oxidative stability window of the eutectic electrolyte in the potential window of open circuit potential (OCP) to 5.0 V, at a scan rate of 0.5 mV s^{-1}, as shown in Figure 3(c). The LSV results indicate that the electrochemical stability limit for the optimized eutectic electrolyte is 2.44 and 2.57 V on the carbon-coat aluminum and molybdenum (Mo) substrates, respectively (see Figure S8). The utilization of eutectic electrolyte with a broad operational potential range overcomes the limitations of hydrogen evolution and enhances the performance of aqueous iron batteries. This makes non-aqueous iron-ion system a promising candidate among multivalent metal batteries.[35]

A symmetric Fe||Fe cell was fabricated in the optimized eutectic electrolyte and subjected to galvanostatic charge−discharge (GCD) analysis at different current rates to assess the stability and reversibility of iron electrodeposition and dissolution. The GCD profiles, as shown in Figure 3(d), were engaged for a duration of 10 min for each charge−discharge cycle. The symmetric Fe||Fe cell exhibited a voltage hysteresis of ∼0.26 V in the first 15 h of cycling at a current density of ∼14 $\mu A\ cm^{-2}$. However, the Coulombic efficiency of iron plating/stripping remained remarkably high (>100%) for the subsequent cycles (up to 50 h). Such occurrence rise in overpotential at higher or lower current densities after the first few hours of cycling hints the surface activation process influencing electrode surface activity for electrochemical reactions.[36−39] The symmetric iron cell exhibits a voltage hysteresis of 0.54 and 0.55 V at current densities of 0.1 mA cm^{-2} and 0.14 mA cm^{-2}, respectively, and demonstrates long-term stability of >400 h under various current densities. To elucidate the electrochemical plating/stripping mechanism, SEM micrographs were acquired on the cycled symmetric iron cell. Representative SEM micrographs of Fe CE is shown in Figure 3(e), and Fe WE is shown in Figure 3(f). From the recorded micrographs, it is evident that the Fe CE undergoes corrosion upon stripping, and Fe WE yield the deposited Fe substrates. The SEM images reveal that the Fe CE suffers from corrosion during stripping and the Fe WE exhibits the nondendritic iron growth. The presence of stable iron deposits on the working electrode (WE) is an encouraging aspect, as it effectively prevents short-circuiting, a common issue in many metal based batteries caused by the growth of needle-like

https://doi.org/10.1021/acsaem.4c00263
ACS Appl. Energy Mater. 2024, 7, 3876−3887

structures known as dendrites.[40,41] X-ray diffraction (XRD) is recorded for pristine Fe foil and the cycled Fe (working electrode) derived from the symmetrical Fe cell (see Supporting Information, Figure S9). Pristine Fe demonstrates a predominant XRD peak aligned with the *(110)* crystal plane, which is the primary exposed crystal plane. In contrast, the cycled Fe electrode exhibits an increased prominence of the *(200)* plane, signifying a shift from *(110)* to *(200)* in the preferred orientation.[42] This shift strongly indicates a (200) preferred orientation in Fe deposition following cycling. Furthermore, the plating/stripping efficiency was examined by assembling an asymmetric Fe||Mo cell and performed GCD analysis as shown in Figure 3(g). The GCD analysis was carried out at different current densities of ~0.09 mA.cm^{-2} and ~0.18 mA.cm^{-2} with an estimated arial capacity of 0.1 mAh cm^{-2}. The cell shows a plating/stripping efficiency of ~82%, which remains as a viable alternative to the existing aqueous electrolyte for iron batteries.[7] The half-cell reaction characteristics of processes that occur on the iron anode are summarized based on the following observations derived from our study: (i) Vibrational spectroscopy identifies the likely ionic species present in the optimized eutectic electrolyte, namely Et_3NH^+, $FeCl_4^-$, and $Fe_2Cl_7^-$; (ii) Evan's method of dc polarization coupled with EIS record of Fe||SS cell estimates a high anionic transference number, reaching close to unity; (iii) Half-cell Fe|| SS 316 and symmetric Fe||Fe cell demonstrates high plating/stripping efficiency; (iv) SEM micrographs of CE and WE from Fe||Fe cell reveal corrosion and Fe plating, respectively. The half-cell reaction at iron anode is

$$Fe + 7FeCl_4^- \leftrightarrow 4Fe_2Cl_7^- + 3e^-$$

The energy density and cell voltage of a battery are governed by all three components of the battery, *i.e.*, anode, electrolyte, and cathode. While the motivation lies in the potential to employ high-capacity-dense multivalent metal anodes, cathodes account for the total energy density output of a battery. V_2O_5 is a well-known transition metal oxide with an approximate interlayer *d*-spacing of 4.4 Å, which provides good structural stability, ease of tunability to vary interlayer spacing, and high working potential.[43] Hence, we selected V_2O_5 as a potential candidate for a cathode against an iron anode. V_2O_5-nanowires are synthesized via a facile hydrothermal synthetic route and a representative SEM image is shown in Figure 4(a). The nanowire exhibits a typical diameter of ~0.35 μm (shown in Figure S10). Figure 4(b) presents the X-ray diffraction pattern of the material after the synthesis and

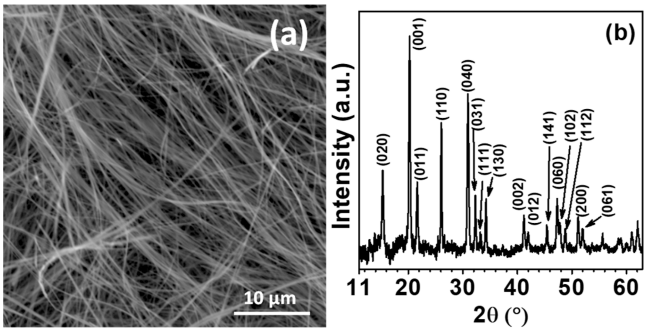

Figure 4. (a) SEM image of hydrothermally synthesized V_2O_5 nanowires and (b) corresponding XRD patterns.

all reflections are indexed to the orthorhombic phase of V_2O_5.[44]

The full cell, comprising an iron anode, a V_2O_5-nanowire cathode, and 1.7:1 $(Et_3NH)Cl:FeCl_3$ electrolyte, was fabricated to evaluate the electrochemical performance. Primarily, CV measurements were performed in the potential window of 0.0−2.5 V vs Fe/Fe^{3+} at different scan rates from 0.5 to 0.1 mV.s^{-1}, as shown in Figure 5(a). Before recording the CV

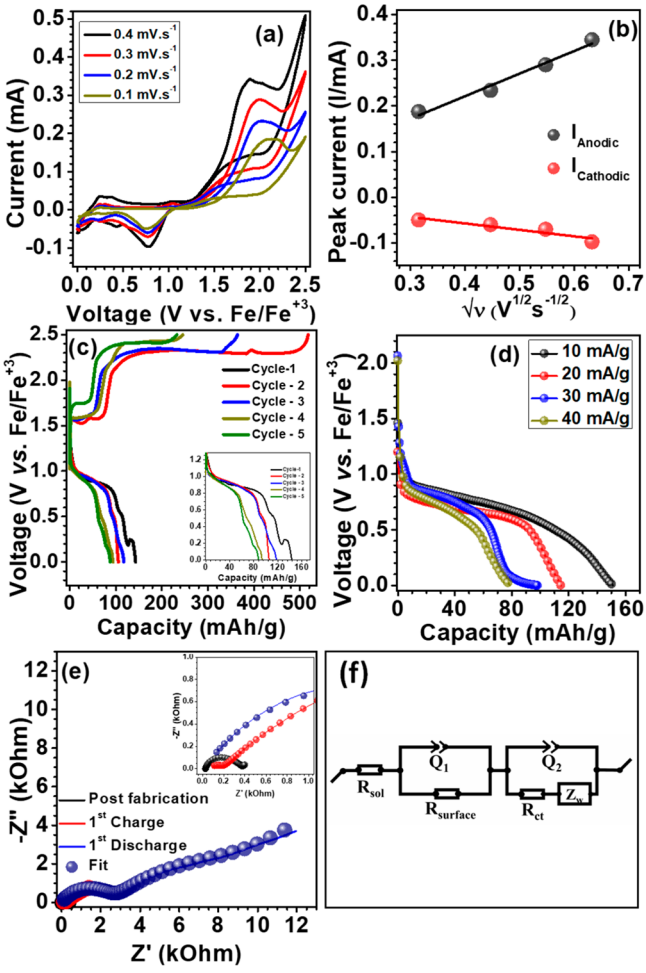

Figure 5. (a) Representative cyclic voltammetric profiles of the V_2O_5 electrode as a function of scan rates. (b) Corresponding linear fits of Ip-anodic and Ip-cathodic data for the estimation of the iron-ion diffusion coefficient for the electrodes. Representative galvanostatic discharge profiles of V_2O_5-nanowire cathodes (c) at 10 mA g^{-1} and (d) at various current densities ranging from 10 to 40 mA g^{-1}. (e) Comparative electrochemical impedance spectroscopies recorded on a V_2O_5 cathode at different stages of cycling and (f) representative equivalent circuit model employed to fit.

patterns at low scan rates, we cycled the Fe||V_2O_5 cell for 10 cycles at 5 mV s^{-1}, to stabilize the host cathode structure through initial phase or interfacial transformations. All CV patterns show a distinct pair of irreversible redox peaks in the wide potential window of 0.3−2.3 V vs. Fe/Fe^{3+}. Moreover, the diffusion coefficient (D, cm^2 s^{-1}) is calculated to understand the diffusion mobility of active ionic species from the electrolyte at the cathode site. Figure 5(b) shows the typical peak current versus $\nu^{1/2}$, derived from CV plots as a function of scan rates. The Randles-Sevcik equation is used to estimate the diffusion coefficient, i.e. $I_p = 0.4463nFAC(nFD/$

https://doi.org/10.1021/acsaem.4c00263
ACS Appl. Energy Mater. 2024, 7, 3876−3887

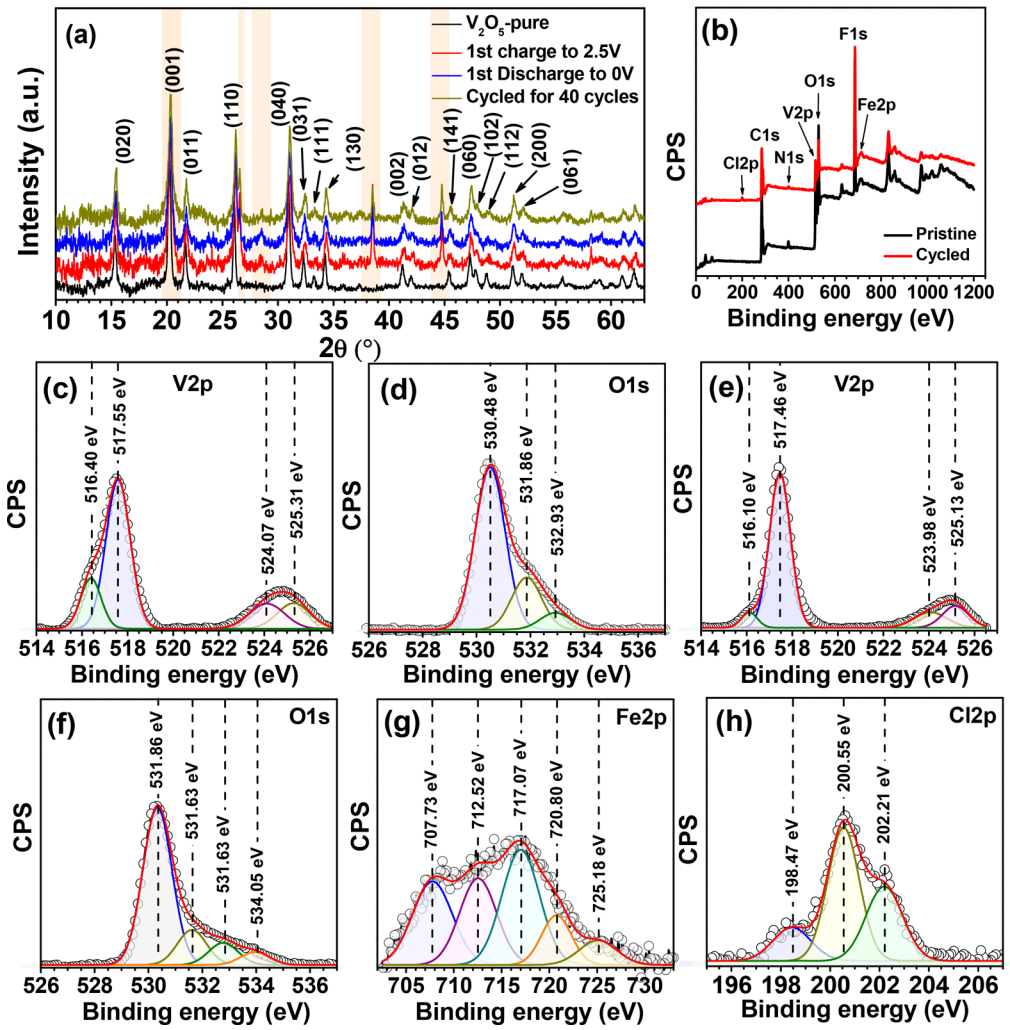

Figure 6. (a) X-ray diffraction patterns were recorded for V_2O_5 electrodes before and postcycling in the 2θ range of ~10−65°. (b) XPS survey scan was recorded for pristine and the cycled V_2O_5 electrode. High-resolution scans for (c) V 2p and (d) O 1s of the pristine V_2O_5 electrode, respectively. High resolution scans were recorded for (e) V 2p, (f) O 1s, (g) Fe 2p, and (h) Cl 2p from the cycled V_2O_5 electrode, respectively.

$RT)^{1/2}\nu^{1/2}$, considering F = 96 485 C mol^{-1}, area (A) = 0.7125 cm^2, temperature (T) = 298 K, and concentration (C) = 0.6 M derived from 1 molar ratio of (Et_3NH)Cl to the concentration of $FeCl_3$ present. The number of electron transfers is considered as 3, according to the half-cell equation proposed for the iron half-cell. The estimated diffusion coefficient at the anodic site is ~5.23 × 10^{-13} cm·s^{-1} and the cathodic site is ~4.25 × 10^{-14} cm·s^{-1}.

The electrochemical performance of Fe||1.7:1-(Et_3NH)-Cl:$FeCl_3$||V_2O_5 cell was comprehensively assessed using the galvanostatic cycling in the potential window of 0.0−2.5 V vs. Fe/Fe^{3+}. The first few GCD cycles at 10 mA g^{-1}, as shown in Figure 5(c), delivered a high discharge capacity of ~150 mAh.g^{-1}. However, the subsequent discharge cycles show a gradual drop in the discharge profile with ~20 mAh g^{-1} retained after 9 cycles, as shown in Figure S11. The cell at different C-rates, as shown in Figure 5(d), demonstrated promising capacity retention of ~150 mAh g^{-1} at the current density of 10 mA g^{-1}. Typical EIS measurements were probed on a stabilized Fe||V_2O_5 cell, postfabrication, and after fully charge or discharge state at rest to understand the interfacial changes that occurred upon first galvanostatic cycling. EIS measurements (Figure 5(e) and Figure S13) were carried in the frequency range of 1 MHz to 50 mHz and the experimental records were appropriately fitted with Randle's equivalent circuit model (Figure 5(f)) where R_{sol} is the solution resistance, $R_{surface}$ is the resistance generated from the electrode interface and R_{ct} is the charge-transfer resistance derived from the electrode−electrolyte interface. Z_w accounts for the Warburg impedance, and the capacitive contributions are accounted by considering the constant phase element (Q). Postfabrication of the Fe||V_2O_5 cell displayed R_{sol} and $R_{surface}$ and R_{ct} of 29 Ohm, 44 Ohm, and 67 Ohm, respectively. The EIS study during the cycling shows a consistent increment of the $R_{surface}$ across cycles, rising from 100 Ohms after the first cycle to 2309 Ohms after the third cycle (see the Supporting Information, Figure S13 and Table S3). This behavior can be rationalized by the accumulation of a solid-electrolyte interphase (SEI) layer growth, which commonly occurs in batteries during cycling of a battery. This layer's formation contributes to enhanced resistance, thus accounting for the observed rise in impedance and attributed to the irreversible capacity loss upon cycling.[45−47] The R_{ct} value of the cell showed a similar trend upon cycling. Nonetheless, the R_{ct} value displayed a lower value of postdischarge compared to the charged state of the electrode. This behavior can be

https://doi.org/10.1021/acsaem.4c00263
ACS Appl. Energy Mater. 2024, 7, 3876−3887

rationalized by the accumulation of SEI upon charge and substantially decompose upon the discharge state.

The charge storage mechanism is determined by the ionic charge carriers from the electrolyte, which dictate the feasible reaction pathways at the cathode interface. The eutectic electrolyte consists of the following types of charge transporters: $(C_2H_5)_3NH^+$, $FeCl_4^-$, and $Fe_2Cl_7^-$. Metal oxides such as V_2O_5 have large *d*-spacing convenient for the interaction of bulk ionic species.[48] However, transition metal oxides also undergo conversion-type reactions in acidic electrolytes.[49] Hence, the battery can be defined as a pure iron-ion battery. To unveil the type of charge storage mechanism, X-ray diffractograms were recorded, as shown in Figure 6(a), for pristine, and cycled V_2O_5 at different states of charge or discharge. All characteristic reflections of orthorhombic-V_2O_5 phase exhibit a significant shift toward higher angles for the charged state and slightly shift toward lower angles for the discharged state, indicating the irreversible charge storage accompanied by the phase change. Nonetheless, few additional reflections detected for all cycled electrodes at ∼26.6°, ∼28.6°, ∼31.6°, ∼38.6°, and ∼44.7°, denote the formation of $Fe_xV_2O_5$.[50−52]

X-ray photoelectron spectroscopy (XPS) was used to provide further evidence and confirm the findings. In XPS, the core level peaks were compared to the carbon edge peak, which has an energy of 284.5 eV. Figure 6(b) illustrates XPS spectra obtained for both the pristine and the cycled V_2O_5 electrode. The V 2p spectra, depicted in Figure 6(c), were deconvoluted into peaks with binding energies maxima at 517.6 eV, 525.3 eV, 516.4 eV, and 524.1 eV, corresponding to the $V^{+5}2p_{3/2}$, $V^{+5}2p_{1/2}$, $V^{+4}2p_{3/2}$, and $V^{+4}2p_{1/2}$ oxidation states, respectively.[53,54] In Figure 6(d), the O 1s band was deconvoluted into three distinct peaks, pointing to the successful formation of V_2O_5 phase. The peaks at ∼530.5 eV and at 531.9 eV correspond to the terminal (=O) and linkage (−O−) oxygen species, respectively.[55] An additional peak observed at ∼532.9 eV is attributed to the presence of hydroxyl oxygen (−OH), which may have originated from the hydrothermal synthesis procedure or due to exposure to ambient humidity.[55,56] Significant changes were observed in the cycled V_2O_5 electrode, as evidenced by a considerable shift in the V 2p and O 1s bands toward lower energy ranges, as shown in Figure 6(e) and (f), respectively. This shift may be attributed to the likely event of V^{+5} (or V^{+4}) reduction to V^{+3} or (V^{+2}).[54,57] The XPS band shift toward lower energy can be rationalized by the interaction of V_2O_5 with Fe-ions such as $Fe_2Cl_7^-$ during charging, resulting in a chemical conversion reaction. However, due to the low-valent and electron-deficient nature of Fe^{3+}, it can only accept electrons from the O 1s band, partially reducing its oxidation state. The proposed mechanism is further supported by the high-resolution spectra presented in Figure 6(g), which were recorded to determine the valence state of Fe. Peaks at 712.4 and 725.2 eV correspond to the Fe^{3+} $2p_{3/2}$ and Fe^{3+} $2p_{1/2}$ states, respectively, while the presence of Cl 2p in the cycled electrode, as shown in Figure 6(h), confirms the Fe^{3+} state from chloroferrate-ions.[29,58] A broad satellite peak at ∼717.1 eV is also attributed to the Fe^{3+} state.[57,59] Additional peaks corresponding to $Fe^{2+}2p_{3/2}$ at 707.7 eV and $Fe^{2+}2p_{1/2}$ at ∼720.8 eV indicate the presence of Fe^{2+}, suggesting the formation of Fe_x-O upon cycling.[60,61] The evidence drawn from the XRD and XPS analysis strongly corroborate the conversion reactions occurring and formation of $Fe_xV_2O_5$ which contributes to the irreversible capacity retention observed in the Fe||V_2O_5 cell.

The plausible charge storage mechanism at the cathode site can be expressed as follows:

$$4Fe_2Cl_7^- + V_2O_5 + 3e^- \leftrightarrow Fe_xV_2O_5 + 7FeCl_4^-$$

SEM micrographs recorded for the pristine V_2O_5 and cycled electrodes, as shown in Figure S12(a) and (b), respectively, reveal porous electrode morphology. No solid electrolyte interfacial components at the cathode are detectable, which is a distinctive feature of the electrolyte.

The development of efficient electrolytes for multivalent metal anodes is hindered by several challenges, such as (i) the strong interaction between the high charge-density metal and the electrolyte species, which slows the diffusion kinetics at the cathode interface; (ii) the passivation of metal anodes, which prevents the reversible plating and stripping process; (iii) electrolyte stability in the presence of multivalent metal ions, which are prone to form ion−ion and ion−solvent complexes that reduce the ion mobility; and (iv) the high energy barriers or overpotentials required for multivalent metal plating and stripping, which result in high energy loss. Despite these challenges, $(Et_3NH)Cl:FeCl_3$ successfully functions as efficient electrolyte media for Fe-ion batteries. However, the electrochemical stability of Fe||SS 316 cell and the cyclability of Fe||V_2O_5 cell in the optimized eutectic electrolyte need to be improved by tuning electrolyte composition and properties.

It has been previously reported that the addition of strong Lewis's acids such as $AlCl_3$ enhances the efficiency and reversibility of electroplating and stripping processes, further extending the electrochemical stability window for multivalent metal batteries.[62] Thus, $AlCl_3$ as an additive to the optimized eutectic electrolyte is anticipated to enhance the electrochemical properties of iron batteries. We observed that increasing $AlCl_3$ concentration in 1.7:1 $(Et_3NH)Cl:FeCl_3$ beyond >1 M led to the formation of a highly viscous phase and beyond 2 M resulted in the solidification of the solution. Hence, we performed all of the electrochemical characterizations using 1 M $AlCl_3$/1.7:1-$(Et_3NH)Cl:FeCl_3$. The primary investigation into the ionic speciation within the electrolyte following the addition of $AlCl_3$ revealed the presence of $AlCl_4^-$ through distinctive peaks in the Raman spectra at 348 cm^{-1}, as shown in Figure S16.[63] Quantification of the relative concentrations utilized Raman peak intensities at 348 cm^{-1} for $AlCl_4^-$ and 334 cm^{-1} for $FeCl_4^-$. The observed ratio of $[AlCl_4^-]/[FeCl_4^-]$ was determined as 0.3.

Typical CV studies were recorded for Fe||SS 316 cell, as depicted in Figure 7(a), in the potential window of −1.0 to 1.0 V vs. Fe/Fe^{3+}, keeping Fe as CE and SS 316 as WE at a slew rate of 0.5 $mV.s^{-1}$. The first cycle shows poor plating/stripping efficiency, but the subsequent cycles demonstrated stabilized cyclability of the Fe anode in the electrolyte composition. LSV measurements for Fe||SS 316 cell in the potential window of OCP to 5 V vs Fe/Fe^{3+} at a scan rate of 0.5 mV s^{-1}, keeping Fe as CE and SS 316 as WE. Unlike the binary phase eutectics, Lewis acid additive significantly enhanced the anodic stability of the electrolyte on SS 316 plate to ∼3.4 V vs Fe/Fe^{3+}, as represented in Figure 7(b). These half-cell results demonstrate the promising properties of the electrolyte for the application of complete Fe-ion cells.

GCD studies were performed on Fe||V_2O_5 cells in 1 M $AlCl_3$/1.7:1-$(Et_3NH)Cl:FeCl_3$, as shown in Figure 7(c), in the potential window of 0.0−2.5 V vs. Fe/Fe^{3+} at a current density

https://doi.org/10.1021/acsaem.4c00263
ACS Appl. Energy Mater. 2024, 7, 3876−3887

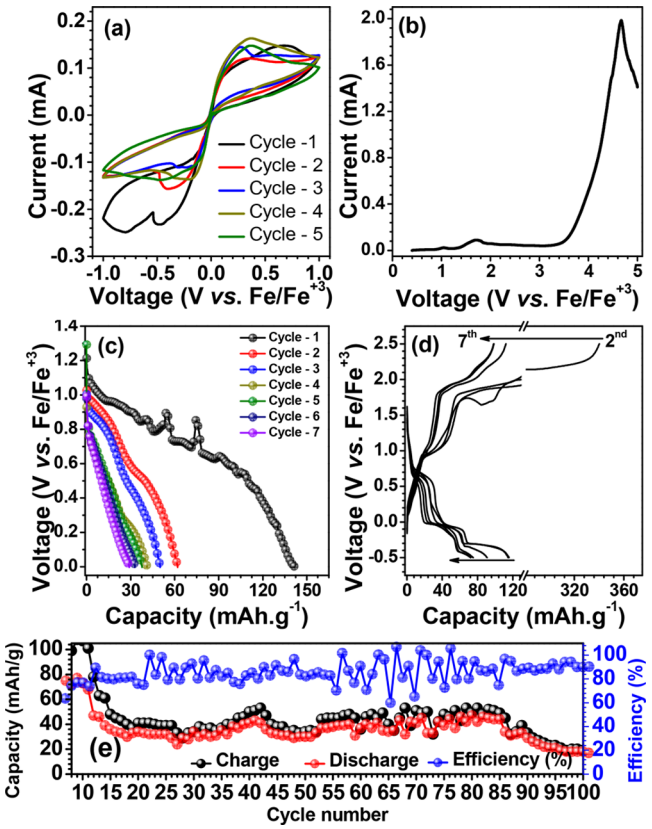

Figure 7. All of the electrochemical characterizations were employed in 1 M $AlCl_3$/1.7:1 $(Et_3NH)Cl$:$FeCl_3$ electrolyte. (a, b) Typical CV plots and LSV plots recorded for Fe||SS 316 cells, respectively, at 0.5 mV s^{-1}. (c, d) Voltage profiles as a function of capacity for Fe||V_2O_5-nanowire at 30 mA g^{-1} and 50 mA g^{-1}, respectively. The onset potential windows for (c) and (d) are executed in 0.0−2.5 V vs. Fe/Fe^{3+} and −0.5−2.5 V vs. Fe/Fe^{3+}, respectively. (e) Typical Fe||V_2O_5-nanowire cell performance at an applied current density of 50 mA g^{-1} recorded for 100 cycles.

of ∼30 mA g^{-1}. Typical discharge voltage as a function of capacity showed ∼140 mAh g^{-1} capacity for the first cycle and ∼30 mAh g^{-1} for the seventh cycle.

The charge-storage mechanism for aqueous iron-ion batteries involves the conversion or plating/stripping of Fe depending on the pH of the aqueous electrolyte.[10] Extending the potential window of Fe||V_2O_5 cell toward a negative voltage profile (i.e., −0.5 V) is anticipated to follow a dual charge-storage mechanism i.e. plating/stripping followed by conversion type. However, with the motivation to improve the cyclability of Fe||V_2O_5 cell, we performed GCD analysis in the potential window of −0.5−2.5 V vs Fe/Fe^{3+}, at an applied current density of ∼50 mA g^{-1}. The first few GCD profiles are shown in Figure 7(d), where a high-capacity retention of ∼120 mAh g^{-1}. However, the efficiency of the cell was poor for the first 3 cycles, which could be attributed to the cathode structural changes or solid electrolyte interphase formation. The efficiency of the subsequent cycles, as shown in Figure 7(e), reached >90% Coulombic efficiency. This report presents the first nonaqueous eutectic electrolyte for rechargeable iron batteries that show promising electrochemical performance comparable to aqueous iron batteries.[10,64,65] Future directions lie in integrating new redox chemistry cathode materials to achieve high performance and reversibility in iron batteries.

CONCLUSIONS

A series of eutectic electrolytes composed of $(Et_3NH)Cl$ and $FeCl_3$ were successfully prepared and optimized for rechargeable Fe-ion battery application. Various properties of the electrolyte were established by using vibrational spectroscopy techniques and electroanalytical techniques. The key ionic complexes present in the electrolytes were identified as $(C_2H_5)_3NH^+$, $FeCl_4^-$, and $Fe_2Cl_7^-$. The electrolyte exhibited appreciably high ionic conductivity (∼1.2 mS cm^{-1}), efficient iron plating/stripping (>82% on SS 316 plate and Mo), high electrochemical stability (∼2.5 V), long-term stability (>400 h) and low melting point at −11 °C. The full cell fabricated using Fe as an anode and V_2O_5-nanowires as a cathode in the optimized eutectic electrolyte delivers ∼150 mAh g^{-1} at 10 mA g^{-1} current density. $AlCl_3$ addition increases the potential window of the eutectic electrolyte by three times on an SS 316 plate and sustains >100 GCD cycles at ∼50 mA g^{-1}. The charge storage mechanism deduced using XRD detects the conversion type redox reaction occurring at the cathode. In summary, the encouraging and reassuring results indicate the potential of eutectic electrolytes for the design of nontoxic, cheap, high-performance, and safe rechargeable iron batteries.

EXPERIMENTAL SECTION

Materials. Triethylamine hydrochloride $[(C_2H_5)_3NH]Cl$ or $(Et_3NH)Cl$ ≥ 99%), anhydrous iron(III) chloride ($FeCl_3$, ∼97%, reagent grade), and poly(vinylidene fluoride) (PVDF powder) were procured from Sigma-Aldrich. Aluminum chloride ($AlCl_3$, anhydrous, 99.985% metal basis) iron foil (99.5% metal basis, 0.025 mm thick), vanadium oxide (V_2O_5, 99.6%, ∼10 mesh), and conductive carbon black is purchased from Thermo Scientific. 1-Methyl-2-pyrrolidinone (C_5H_9NO, 99.5%) procured from Spectrum Chemical Manufacturing Corporation. Hydrogen peroxide (H_2O_2, 30% solution) and hydrochloric acid (HCl) were purchased from EMD Millipore Corporation. Carbon-coated aluminum foil (∼16 μm thickness) was procured from MTI Corporation. Ethyl alcohol (C_2H_5OH) was purchased from KOPTEC.

Synthesis of V_2O_5 Nanowires. V_2O_5 nanowires synthesis followed via facile hydrothermal method.[66] In a typical synthetic procedure, 0.364g of V_2O_5 was dissolved in 30 mL of deionized water under constant stirring at room temperature. 5 mL of 30% H_2O_2 solution is added to the above prepared V_2O_5/H_2O yellow suspension dropwise for 30 min under constant stirring until a clear ruby red colored solution is obtained. Further, the solution is transferred to a 40 mL of Teflon-lined stainless-steel autoclave and heated at 205 °C for 96 h. A fibrous texture containing yellow product is obtained, and it is washed with ethanol, followed by distilled water (2 times), and dried at 100 °C for 12 h. The final product is obtained at 500 °C for 4 h.

Eutectic Electrolyte Preparation. A series of eutectic electrolytes prepared iteratively by mixing various molar ratios of $(Et_3NH)Cl$ to $FeCl_3$ in stoichiometries of 1.5, 1.6, 1.7, 1.8, 1.9, and 2.0:1 in an argon-filled Glovebox (<0.01 ppm of O_2, <0.01 ppm of H_2O, Vacuum Technology Inc.), under constant stirring at room temperature. The electrolytes were kept under stirring for the next 24 h, and the compositions which retained the liquid phase are further assessed for *physicochemical* and electrochemical properties.

Computational Details. The first-principles calculations in this study were performed using the Vienna Ab initio Simulation Package VASP 5.4.4 based on the projector augmented wave (PAW) potentials.[67−69] A plane-wave basis set with a cutoff energy of 400 eV and a Gamma centered 1 × 1 × 1 K point mesh were applied for geometry optimization and charge density calculation. The ions were relaxed using conjugate gradient algorithm with force and energy convergence criteria of −0.03 eV/Å and 10^{-5} eV, respectively.

Electrode Preparation. V_2O_5 nanowire electrodes are prepared by ball-milling an appropriate weight ratio of V_2O_5 nanowires: Super-

https://doi.org/10.1021/acsaem.4c00263
ACS Appl. Energy Mater. 2024, 7, 3876−3887

P conductive carbon: PVDF (80:10:10 wt %, respectively) for 3 h at 300 rotations per minute, followed by mixing with 1-methyl-2-pyrrolidone solvent. The obtained homogeneous slurry is cast on the carbon-coat Al current collector and dried under vacuum for 12 h at 100 °C. The dried electrodes are used as positive electrodes in a full-cell fabrication.

Materials Characterization. Functional group identification and probable inter- and/or intramolecular interactions are characterized using FT-IR (The Nicolet 6700 FTIR Spectrometer), in the range of ∼4000−400 cm^{-1} by averaging 64 scans with a resolution of ∼2 cm^{-1}. Raman spectroscopy is employed to decipher the ionic complexes present in the electrolytes in the range 50−3200 cm^{-1}, on a WITec Alpha300R instrument. X-ray diffraction studies were carried out on Rigaku SmartLab X-ray diffractometer. Scanning Electron Microscopy employed (TESCAN VEGA with an accelerating voltage of 20 kV) on the cycled electrodes from Fe||Fe cell and V_2O_5 electrodes (postfabrication and after cycling) synthesized sample to evaluate the morphology and the structural changes. DSC data were obtained using Netzsch STA 449 F3 Jupiter TGA/DSC instrument; ∼15 mg of electrolyte was sealed in an aluminum crucible under nitrogen and transferred onto the instrument. The instrument was cooled to ∼150 °C and the data was recorded upon sample warming to 25 °C at 5 °C/min. The binding energy of electrodes were assessed using X-ray Photoelectron Spectroscopy on a Kratos AXIS ULTRA X-ray Photoelectron Spectrometer.

Electrochemical Properties Assessment. All test cells are fabricated using a coin cell 2032 in the Ar-filled glovebox (<0.01 ppm of O_2 and <0.01 ppm of H_2O, Vacuum Technologies Inc. made). The electrochemical performance of half-cells and full-cells was evaluated using a multichannel Biologic VSP Potentiostat (EC-Lab v11.30 software) for all measurements except the galvanostatic charge−discharge cycling tests, which were conducted on a multichannel Neware Battery Testing System (BTS v8 software).

Half-cells (symmetric or asymmetric, i.e., SS||SS, Fe||SS, Fe||Fe) were assembled using the electrodes with a diameter of ∼0.9525 cm in a coin cell 2032 and a Teflon separator having 0.005″ thickness is introduced between the electrodes. Electrochemical Impedance Spectroscopy was performed on the symmetric SS||SS cell in the frequency range of 1 MHz to 1 kHz at open circuit potential and amplitude of ±10 mV. Ionic and electronic transport numbers are evaluated by applying a DC potential of 100 mV and 1 V to measure the current as a function of time. Ionic and electronic transference numbers of the electrolyte are characterized on an Fe||SS-316 cell, by implying an EIS study before and after the polarization at different potentials (100 mV and 1 V). The Fe electrode stability in the electrolyte is investigated by fabricating a symmetric Fe||Fe cell and engaged galvanostatic charge−discharge (GCD) analysis at different current densities (14 $\mu A\ cm^{-2}$ to 0.14 $mA\ cm^{-2}$) in the potential window of −1.5 to 1.5 V vs. Fe/Fe^{3+}. Plating/stripping of the Fe electrode on the SS plate is investigated by fabricating an asymmetric Fe||SS cell, in the potential window of −0.5 to 0.5 V vs. Fe/Fe^{3+} at a slew rate of 0.5 mV s^{-1}. The stability of the electrolyte on different substrates such as SS 316 or carbon-coated Al or molybdenum is measured by fabricating an asymmetric cell and recorded linear sweep voltammetry in the potential window of the OCP to 5.0 V vs Fe/Fe^{3+}, at a scan rate of 0.5 mV s^{-1}. Here, Fe is considered as a counter electrode (CE), and the SS-316 plate is used as a working electrode (WE). The plating and stripping efficiency is measured by fabricating an Fe||Mo cell (Fe as CE and Mo as WE) and employing GCD in the potential window of −1.5 to 1.5 V vs. Fe/Fe^{3+}.

Full-cell electrochemical performance is evaluated by fabricating a Fe||V_2O_5 cell in the optimized eutectic electrolyte, and a 934-AH glass fiber (Whatman) is used as a separator. Cyclic voltammetry and GCD of the cell are performed in the voltage range of 0.0−2.5 V vs. Fe/Fe^{3+}. EIS coupled with GCD of the full cell is performed in the frequency range of 1 MHz to 50 mHz at different states of the cell (postfabrication or charge or discharge) at rest.

■ ASSOCIATED CONTENT

Supporting Information

The Supporting Information is available free of charge at https://pubs.acs.org/doi/10.1021/acsaem.4c00263.

The chronoamperometric plots, Raman spectroscopy, cyclic voltammetry of half-cells, galvanostatic charge−discharge performance of half-cells, XRD patterns of Fe deposition, SEM of synthesized V_2O_5 wires post synthesis and cycling, impedance, and X-ray photoelectron spectroscopies of Fe−V_2O_5 cell at various stages of GCD analysis (PDF)

■ AUTHOR INFORMATION

Corresponding Author

Shuya Wei − *Department of Chemical and Biological Engineering, University of New Mexico, Albuquerque, New Mexico 87131, United States;* orcid.org/0000-0001-9269-1950; Email: swei@unm.edu

Authors

Raju Vadthya − *Department of Chemical and Biological Engineering, University of New Mexico, Albuquerque, New Mexico 87131, United States*

Nikhitha Poornabodha − *School for Engineering of Matter, Transport and Energy, Arizona State University, Tempe, Arizona 75281, United States*

Hao Nguyen − *Department of Chemical and Biological Engineering, University of New Mexico, Albuquerque, New Mexico 87131, United States;* orcid.org/0009-0002-8655-2692

Olumide Oladoyin − *Department of Chemical and Biological Engineering, University of New Mexico, Albuquerque, New Mexico 87131, United States*

Sergei A Ivanov − *Materials Physics and Applications Division and Center for Integrated Nanotechnologies, Los Alamos National Laboratory, Los Alamos, New Mexico 87545, United States;* orcid.org/0000-0001-6790-5187

Houlong Zhuang − *School for Engineering of Matter, Transport and Energy, Arizona State University, Tempe, Arizona 75281, United States*

Complete contact information is available at: https://pubs.acs.org/10.1021/acsaem.4c00263

Author Contributions

The manuscript was written through contributions of all authors. All authors have given approval to the final version of the manuscript.

Funding

This work was supported by National Aeronautics & Space Administration under Award Number 80NSSC23M0151 and National Science Foundation under Award Number 2119688. S.W. acknowledges the startup support from the University of New Mexico. This work was performed, in part, at the Center for Integrated Nanotechnologies, an Office of Science User Facility operated for the U.S. Department of Energy (DOE) Office of Science. Los Alamos National Laboratory, an affirmative action equal opportunity employer, is managed by Triad National Security, LLC for the U.S. Department of Energy's NNSA, under contract 89233218CNA000001.

Notes

The authors declare no competing financial interest.

REFERENCES

(1) Diouf, B.; Pode, R. Potential of Lithium-Ion Batteries in Renewable Energy. *Renew. Energy* **2015**, *76*, 375−380.
(2) Zu, C.-X.; Li, H. Thermodynamic Analysis on Energy Densities of Batteries. *Energy Environ. Sci.* **2011**, *4* (8), 2614−2624.
(3) Rodrigues, M.-T. F.; Babu, G.; Gullapalli, H.; Kalaga, K.; Sayed, F. N.; Kato, K.; Joyner, J.; Ajayan, P. M. A Materials Perspective on Li-Ion Batteries at Extreme Temperatures. *Nat. Energy* **2017**, *2* (8), 1−14.
(4) Xie, J.; Zhang, Q. Recent Progress in Multivalent Metal (Mg, Zn, Ca, and Al) and Metal-Ion Rechargeable Batteries with Organic Materials as Promising Electrodes. *Small* **2019**, *15* (15), No. 1805061.
(5) Liang, Y.; Dong, H.; Aurbach, D.; Yao, Y. Current Status and Future Directions of Multivalent Metal-Ion Batteries. *Nat. Energy* **2020**, *5* (9), 646−656.
(6) Fetrow, C.; Carugati, C.; Yu, X.; Zhou, X.-D.; Wei, S. A Secondary Al−CO_2 Battery Enabled by Aluminum Iodide as a Homogeneous Redox Mediator. *ACS Appl. Mater. Interfaces* **2023**, *15* (10), 12908−12914.
(7) Wu, X.; Markir, A.; Xu, Y.; Zhang, C.; Leonard, D. P.; Shin, W.; Ji, X. A Rechargeable Battery with an Iron Metal Anode. *Adv. Funct. Mater.* **2019**, *29* (20), No. 1900911.
(8) Frey, P. A.; Reed, G. H. The Ubiquity of Iron. *ACS Chem. Biol.* **2012**, *7* (9), 1477−1481.
(9) Zhang, H.; Qiao, L.; Kühnle, H.; Figgemeier, E.; Armand, M.; Eshetu, G. G. From Lithium to Emerging Mono- and Multivalent-Cation-Based Rechargeable Batteries: Non-Aqueous Organic Electrolyte and Interphase Perspectives. *Energy Environ. Sci.* **2023**, *16* (1), 11−52.
(10) He, Z.; Xiong, F.; Tan, S.; Yao, X.; Zhang, C.; An, Q. Iron Metal Anode for Aqueous Rechargeable Batteries. *Mater. Today Adv.* **2021**, *11*, No. 100156.
(11) Chai, S.; Zhu, J.; Jiang, J.; Li, C. M. Elevating Kinetics of Passivated Fe Anodes with NH_4Cl Regulator: Toward Low-Cost, Long-Cyclic and Green Cathode-Free Fe-Ion Aqueous Batteries. *Nano Res.* **2022**, *15* (4), 3187−3194.
(12) Xu, Y.; Wu, X.; Sandstrom, S. K.; Hong, J. J.; Jiang, H.; Chen, X.; Ji, X. Fe-Ion Bolted $VOPO_4$•$2H_2O$ as an Aqueous Fe-Ion Battery Electrode. *Adv. Mater.* **2021**, *33* (49), No. 2105234.
(13) Li, C.; Xu, Y.; Deng, W.; Zhou, Y.; Guo, X.; Chen, Y.; Li, R. Regulating Interlayer-Spacing of Vanadium Phosphates for High-Capacity and Long-Life Aqueous Iron-Ion Batteries. *Small* **2024**, *20*, No. 2305766.
(14) Lv, H.; Wei, Z.; Han, C.; Yang, X.; Tang, Z.; Zhang, Y.; Zhi, C.; Li, H. Cross-Linked Polyaniline for Production of Long Lifespan Aqueous Iron||organic Batteries with Electrochromic Properties. *Nat. Commun.* **2023**, *14* (1), 3117.
(15) Vijaya Kumar Saroja, A. P.; Samantaray, S. S.; Sundara, R. A Room Temperature Multivalent Rechargeable Iron Ion Battery with an Ether Based Electrolyte: A New Type of Post-Lithium Ion Battery. *Chem. Commun.* **2019**, *55* (70), 10416−10419.
(16) Zhao, Y.; Zhen, Y.; Boström, T. Rechargeable Iron-Ion Battery Using a Pure Ionic Liquid Electrolyte. *ACS Omega* **2022**, *7* (28), 24082−24090.
(17) Yu, D.; Xue, Z.; Mu, T. Eutectics: Formation, Properties, and Applications. *Chem. Soc. Rev.* **2021**, *50* (15), 8596−8638.
(18) Raju, V.; Madhu Krishna, M.; Kumar Y, V. N.; Jetti, V. R.; Basak, P. Unexplored Class of Eutectic Electrolytes for Rechargeable Magnesium Batteries. *ACS Appl. Energy Mater.* **2022**, *5* (12), 15188−15198.
(19) Nakanishi, K.; Goto, T.; Ohashi, M. Infrared Spectra of Organic Ammonium Compounds. *BCSJ.* **1957**, *30* (4), 403−408.
(20) Birchall, T.; Morris, M. F. Mössbauer and Infrared Spectra of Tetrahedral Complexes of Iron(II) Halides with Thioamides and Related Ligands. *Can. J. Chem.* **1972**, *50* (2), 211−216.
(21) Wagner, J. P.; McDonald, D. C.; Colley, J. E.; Franke, P. R.; Duncan, M. A. Infrared Spectroscopy of the Protonated HCl Dimer and Trimer. *J. Chem. Phys.* **2021**, *155* (13), No. 134302.
(22) Liang, Y.-H.; Wang, C.-C.; Chen, C.-Y. Synthesis and Characterization of a New Network Polymer Electrolyte Containing Polyether in the Main Chains and Side Chains. *Eur. Polym. J.* **2008**, *44* (7), 2376−2384.
(23) Digar, M.; Hung, S. L.; Wang, H. L.; Wen, T. C.; Gopalan, A. Study of Ionic Conductivity and Microstructure of a Cross-Linked Polyurethane Acrylate Electrolyte. *Polymer* **2002**, *43* (3), 681−691.
(24) Li, M.; Guan, J.; Han, J.; Liang, W.; Wang, K.; Duan, E.; Guo, B. Absorption and Oxidation of H2S in Triethylamine Hydrochloride·ferric Chloride Ionic Liquids. *J. Mol. Liq.* **2015**, *209*, 58−61.
(25) Tsuboi, M. 15N Isotope Effects on the Vibrational Frequencies of Aniline and Assignments of the Frequencies of Its Nh2 Group. *Spectrochim. Acta* **1960**, *16* (4), 505−512.
(26) Raju, V.; Rani, J. V.; Basak, P. One-Dimensional Polythiophene/Multi-Walled Carbon Nanotube Composite Cathodes for Rechargeable Magnesium Battery: Evidence of Improved Stability and Electrochemically Induced Rearrangement in Electrode Morphology. *Electrochim. Acta* **2022**, *404*, No. 139707.
(27) Yang, H.; Liu, W.; Wu, F.; Zheng, L.; Bai, Y.; Wu, C. Liquid-State Cathode Enabling a High-Voltage and Air-Stable Fe-Al Hybrid Battery. *Adv. Funct. Mater.* **2023**, *33*, No. 2301006.
(28) Pigorsch, E. Spectroscopic Characterisation of Cationic Quaternary Ammonium Starches. *Starch - Stärke* **2009**, *61* (3−4), 129−138.
(29) Khan, M. U.; Rather, R. A.; Siddiqui, Z. N. Design, Characterization and Catalytic Evaluation of Halometallic Ionic Liquid Incorporated Nd2O3 Nanoparticles ([Smim][$FeCl_4$]−@Nd_2O_3) for the Synthesis of N-Aryl Indeno Pyrrole Derivatives. *RSC Adv.* **2020**, *10* (73), 44892−44902.
(30) Sitze, M. S.; Schreiter, E. R.; Patterson, E. V.; Freeman, R. G. Ionic Liquids Based on $FeCl_3$ and FeCl2. Raman Scattering and Ab Initio Calculations. *Inorg. Chem.* **2001**, *40* (10), 2298−2304.
(31) Francis, C. F. J.; Kyratzis, I. L.; Best, A. S. Lithium-Ion Battery Separators for Ionic-Liquid Electrolytes: A Review. *Adv. Mater.* **2020**, *32* (18), No. 1904205.
(32) Zhu, N.; Zhang, K.; Wu, F.; Bai, Y.; Wu, C. Ionic Liquid-Based Electrolytes for Aluminum/Magnesium/Sodium-Ion Batteries. *Energy Mater. Adv.* **2021**, *2021*, No. 9204217.
(33) Shigenobu, K.; Dokko, K.; Watanabe, M.; Ueno, K. Solvent Effects on Li Ion Transference Number and Dynamic Ion Correlations in Glyme- and Sulfolane-Based Molten Li Salt Solvates. *Phys. Chem. Chem. Phys.* **2020**, *22* (27), 15214−15221.
(34) Shen, C.; Zhao, Q.; Shan, N.; Jing, B. B.; Evans, C. M. Conductivity−Modulus−Tg Relationships in Solvent-Free, Single Lithium Ion Conducting Network Electrolytes. *J. Polym. Sci.* **2020**, *58* (17), 2376−2388.
(35) Zhang, S.; Long, T.; Zhang, H.-Z.; Zhao, Q.-Y.; Zhang, F.; Wu, X.-W.; Zeng, X.-X. Electrolytes for Multivalent Metal-Ion Batteries: Current Status and Future Prospect. *ChemSusChem* **2022**, *15* (21), No. e202200999.
(36) Powell, M.; Wei, S. Surface Characterization and Optimization of Porous Zinc Anodes to Improve Cycle Stability by Mitigating Dendritic Growth. *J. Electrochem. Soc.* **2022**, *169* (10), No. 100511.
(37) Yang, Z.; Zhang, Q.; Xie, C.; Li, Y.; Li, W.; Wu, T.; Tang, Y.; Wang, H. Electrochemical Interface Reconstruction to Eliminate Surface Heterogeneity for Dendrite-Free Zinc Anodes. *Energy Storage Mater.* **2022**, *47*, 319−326.
(38) Zhao, K.; Wang, C.; Yu, Y.; Yan, M.; Wei, Q.; He, P.; Dong, Y.; Zhang, Z.; Wang, X.; Mai, L. Ultrathin Surface Coating Enables Stabilized Zinc Metal Anode. *Adv. Mater. Interfaces* **2018**, *5* (16), No. 1800848.
(39) Zhang, N.; Cheng, F.; Liu, Y.; Zhao, Q.; Lei, K.; Chen, C.; Liu, X.; Chen, J. Cation-Deficient Spinel ZnMn2O4 Cathode in Zn(CF3SO3)2 Electrolyte for Rechargeable Aqueous Zn-Ion Battery. *J. Am. Chem. Soc.* **2016**, *138* (39), 12894−12901.
(40) Zhang, L.; Zhang, B.; Zhang, T.; Li, T.; Shi, T.; Li, W.; Shen, T.; Huang, X.; Xu, J.; Zhang, X.; Wang, Z.; Hou, Y. Eliminating Dendrites and Side Reactions via a Multifunctional ZnSe Protective

https://doi.org/10.1021/acsaem.4c00263
ACS Appl. Energy Mater. 2024, 7, 3876−3887

Layer toward Advanced Aqueous Zn Metal Batteries. *Adv. Functional Mater.* **2021**, *31* (26), No. 2100186.
(41) Wang, T.; Salvatierra, R. V.; Tour, J. M. Detecting Li Dendrites in a Two-Electrode Battery System. *Adv. Mater.* **2019**, *31* (14), No. 1807405.
(42) Zhang, Y.; Zhao, P.; Nie, Q.; Li, Y.; Guo, R.; Hong, Y.; Deng, J.; Song, J. Enabling 420 Wh kg−1 Stable Lithium-Metal Pouch Cells by Lanthanum Doping. *Adv. Mater.* **2023**, *35* (15), No. 2211032.
(43) Natarajan, S.; Kim, S.-J.; Aravindan, V. Restricted Lithiation into a Layered V2O5 Cathode towards Building "Rocking-Chair" Type Li-Ion Batteries and Beyond. *J. Mater. Chem. A* **2020**, *8* (19), 9483−9495.
(44) Zhu, Y.; Yang, M.; Huang, Q.; Wang, D.; Yu, R.; Wang, J.; Zheng, Z.; Wang, D. V2O5 Textile Cathodes with High Capacity and Stability for Flexible Lithium-Ion Batteries. *Adv. Mater.* **2020**, *32* (7), No. 1906205.
(45) Choi, W.; Shin, H.-C.; Kim, J. M.; Choi, J.-Y.; Yoon, W.-S. Modeling and Applications of Electrochemical Impedance Spectroscopy (EIS) for Lithium-Ion Batteries. *J. Electrochem. Sci. Technol.* **2020**, *11* (1), 1−13.
(46) Zheng, Y.; He, Y.-B.; Qian, K.; Li, B.; Wang, X.; Li, J.; Miao, C.; Kang, F. Effects of State of Charge on the Degradation of LiFePO4/Graphite Batteries during Accelerated Storage Test. *J. Alloys Compd.* **2015**, *639*, 406−414.
(47) Mandli, A. R.; Kaushik, A.; Patil, R. S.; Naha, A.; Hariharan, K. S.; Kolake, S. M.; Han, S.; Choi, W. Analysis of the Effect of Resistance Increase on the Capacity Fade of Lithium Ion Batteries. *Int. J. Energy Res.* **2019**, *43* (6), 2044−2056.
(48) Fu, Q.; Zhao, H.; Sarapulova, A.; Dsoke, S. V_2O_5 as a Versatile Electrode Material for Postlithium Energy Storage Systems. *Appl. Res.* **2023**, *2* (3), No. e202200070.
(49) Meng, J.; Zhu, L.; Haruna, A. B.; Ozoemena, K. I.; Pang, Q. Charge Storage Mechanisms of Cathode Materials in Rechargeable Aluminum Batteries. *Sci. China Chem.* **2021**, *64* (11), 1888−1907.
(50) Wang, J.; Chen, Q.; Zeng, C.; Hou, B. Magnetic-Field-Induced Growth of Single-Crystalline Fe3O4 Nanowires. *Adv. Mater.* **2004**, *16* (2), 137−140.
(51) Zhang, J.; Shang, X.; Ren, H.; Chi, J.; Fu, H.; Dong, B.; Liu, C.; Chai, Y. Modulation of Inverse Spinel Fe_3O_4 by Phosphorus Doping as an Industrially Promising Electrocatalyst for Hydrogen Evolution. *Adv. Mater.* **2019**, *31* (52), No. 1905107.
(52) Maingot, S.; Baddour, R.; Pereira-Ramos, J. P.; Baffier, N.; Willmann, P. A New Iron V_2O_5 Bronze as Electrode Material for Rechargeable Lithium Batteries. *J. Electrochem. Soc.* **1993**, *140* (11), L158.
(53) Yi, T.-F.; Qiu, L.; Qu, J.-P.; Liu, H.; Zhang, J.-H.; Zhu, Y.-R. Towards High-Performance Cathodes: Design and Energy Storage Mechanism of Vanadium Oxides-Based Materials for Aqueous Zn-Ion Batteries. *Coord. Chem. Rev.* **2021**, *446*, No. 214124.
(54) Mendialdua, J.; Casanova, R.; Barbaux, Y. XPS Studies of V_2O_5, V_6O_{13}, VO_2 and V_2O_3. *J. Electron Spectrosc. Relat. Phenom.* **1995**, *71* (3), 249−261.
(55) Pradeep, I.; Ranjith Kumar, E.; Suriyanaranan, N.; Srinivas, Ch.; Venkata Rao, N. Structural, Optical and Electrical Properties of Pure and Fe Doped V_2O_5 Nanoparticles for Junction Diode Fabrications. *J. Mater. Sci: Mater. Electron* **2018**, *29* (12), 9840−9853.
(56) Liu, X.; Liu, C.; Wang, Z.; Chen, H.; Liu, Z.; Yang, J.; Lau, W.-M.; Zhou, D. Facile Hydrothermal Synthesis of V_2O_5 Nanofibers as Cathode Material for Aqueous Zinc-Ion Batteries. *J. Alloys Compd.* **2022**, *896*, No. 163071.
(57) Zhang, N.; Zhang, G.; Shen, P.; Zhang, H.; Ma, D.; Chu, K. Lewis Acid Fe-V Pairs Promote Nitrate Electroreduction to Ammonia. *Adv. Funct. Mater.* **2023**, *33* (13), No. 2211537.
(58) Luo, W.; Huang, Q.; Zeng, P.; Cheng, C.; Yuan, X.; Xiao, T.; Zhang, M.; Antwi, P.; Xing, J.; Ren, S. Gemini Surfactant-Modified Montmorillonite with Tetrachloroferrate (FeCl4−) as a Counterion Simultaneously Sequesters Nitrate and Phosphate from Aqueous Solution. *J. Hazard. Mater.* **2021**, *409*, No. 124829.
(59) Zhong, Y.; Ma, Y.; Guo, Q.; Liu, J.; Wang, Y.; Yang, M.; Xia, H. Controllable Synthesis of TiO2@Fe2O3 Core-Shell Nanotube Arrays with Double-Wall Coating as Superb Lithium-Ion Battery Anodes. *Sci. Rep.* **2017**, *7* (1), No. 40927.
(60) Tie, S.-L.; Lee, H.-C.; Bae, Y.-S.; Kim, M.-B.; Lee, K.; Lee, C.-H. Monodisperse Fe_3O_4/Fe@SiO_2 Core/Shell Nanoparticles with Enhanced Magnetic Property. *Colloids Surf., A* **2007**, *293* (1), 278−285.
(61) Yamashita, T.; Hayes, P. Analysis of XPS Spectra of Fe^{2+} and Fe^{3+} Ions in Oxide Materials. *Appl. Surf. Sci.* **2008**, *254* (8), 2441−2449.
(62) Deivanayagam, R.; Ingram, B. J.; Shahbazian-Yassar, R. Progress in Development of Electrolytes for Magnesium Batteries. *Energy Stor. Mater.* **2019**, *21*, 136−153.
(63) Zhu, G.; Angell, M.; Pan, C.-J.; Lin, M.-C.; Chen, H.; Huang, C.-J.; Lin, J.; Achazi, A. J.; Kaghazchi, P.; Hwang, B.-J.; Dai, H. Rechargeable Aluminum Batteries: Effects of Cations in Ionic Liquid Electrolytes. *RSC Adv.* **2019**, *9* (20), 11322−11330.
(64) Hayashi, K.; Wada, Y.; Maeda, Y.; Suzuki, T.; Sakamoto, H.; Tan, W. K.; Kawamura, G.; Muto, H.; Matsuda, A. Electrochemical Performance of Sintered Porous Negative Electrodes Fabricated with Atomized Powders for Iron-Based Alkaline Rechargeable Batteries. *J. Electrochem. Soc.* **2017**, *164* (9), A2049.
(65) Posada, J. O. G.; Hall, P. J. Towards the Development of Safe and Commercially Viable Nickel−Iron Batteries: Improvements to Coulombic Efficiency at High Iron Sulphide Electrode Formulations. *J. Appl. Electrochem.* **2016**, *46* (4), 451−458.
(66) Zhai, T.; Liu, H.; Li, H.; Fang, X.; Liao, M.; Li, L.; Zhou, H.; Koide, Y.; Bando, Y.; Golberg, D. Centimeter-Long V2O5 Nanowires: From Synthesis to Field-Emission, Electrochemical, Electrical Transport, and Photoconductive Properties. *Adv. Mater.* **2010**, *22* (23), 2547−2552.
(67) Kresse, G.; Furthmüller, J. Efficient Iterative Schemes for Ab Initio Total-Energy Calculations Using a Plane-Wave Basis Set. *Phys. Rev. B* **1996**, *54* (16), 11169−11186.
(68) Kresse, G.; Joubert, D. From Ultrasoft Pseudopotentials to the Projector Augmented-Wave Method. *Phys. Rev. B* **1999**, *59* (3), 1758−1775.
(69) Blöchl, P. E. Projector Augmented-Wave Method. *Phys. Rev. B* **1994**, *50* (24), 17953−17979.

https://doi.org/10.1021/acsaem.4c00263
ACS Appl. Energy Mater. 2024, 7, 3876−3887